Dual-space approach for density-functional calculations of two- and three-dimensional crystals using Gaussian basis functions

Xiaojie Chen, Jean-Marc Langlois,* and William A. Goddard III†
Materials and Molecular Simulation Center, Beckman Institute (139-74), Division of Chemistry and Chemical Engineering (CN9042), California Institute of Technology, Pasadena, California 91125
(Received 3 January 1995; revised manuscript received 30 March 1995)

We reformulate theories for electronic structure calculations of periodic systems in a way suitable for large scale calculations using Gaussian basis functions. An accurate grid is introduced for efficient calculation of matrix elements. A dual-space approach is used to calculate the Coulomb potential with computational cost that scales linearly with the size of basis set. A preconditioned generalized conjugate gradients approach is introduced for rapidly converging wave functions expressed in terms of Gaussian basis functions. This method is applied to a variety of crystals (including diamond, GaN, AlN, CdTe, and C_{60}) and surfaces [including GaAs (110) and BN (110)] with excellent results.

I. INTRODUCTION

Density-functional theory (DFT), particularly in the local-density approximation (LDA),[1] has been applied with considerable success to investigate the properties of molecules and solids. In the LDA the electronic ground-state energy E_0 is given by

$$E_0[\{\psi_i\}]=2\sum_i \int d\mathbf{r}\,\psi_i(-\tfrac{1}{2}\nabla^2)\psi_i+\int d\mathbf{r}\,V_{\rm nuc}(\mathbf{r})\rho(\mathbf{r}) +\tfrac{1}{2}\int d\mathbf{r}\,V_{\rm Coul}(\mathbf{r})\rho(\mathbf{r})+E_{\rm xc}[\rho(\mathbf{r})]\ , \quad (1)$$

where for simplicity we consider a closed-shell system (using Hartree atomic units). Here $V_{\rm nuc}$ is the nuclear potential, $V_{\rm Coul}$ is the Coulomb potential, and $E_{\rm xc}$ is the electronic exchange-correlation energy functional (approximated as a function of density). The one-particle wave functions $\{\psi_i(\mathbf{r})\}$ are determined through the Kohn-Sham[1] equation

$$F^{ks}\psi_i(\mathbf{r})=\{(-\tfrac{1}{2}\nabla^2)+V_{\rm nuc}(\mathbf{r})+V_{\rm Coul}(\mathbf{r})+V_{\rm xc}(\mathbf{r})\} \times\psi_i(\mathbf{r})=\epsilon_i\psi_i(\mathbf{r})\ . \quad (2)$$

The density is given by the squared sum of occupied orbitals

$$\rho(\mathbf{r})=2\sum_i^{\rm occ}|\psi_i(\mathbf{r})|^2\ , \quad (3)$$

and the exchange-correlation potential $V_{\rm xc}(\mathbf{r})$ is given by

$$V_{\rm xc}=\frac{dE_{\rm xc}[\rho(\mathbf{r})]}{d\rho(\mathbf{r})}\ . \quad (4)$$

In such first-principles calculations, the most expensive steps are (a) construction of the Coulomb potential ($V_{\rm Coul}$), (b) construction of the Fock operator (F^{ks}), and (c) update of the wave functions. The bottleneck for very large-scale calculations is the cost of updating the wave functions, which scales at least quadratically with the size of the basis set. Consequently it is essential to use the most efficient basis set for representing the electronic wave functions. Among the common basis sets (Gaussian functions, plane wave, augmented plane waves, and muffin-tin orbitals), Gaussian basis sets lead to the most compact size for high accuracy. Indeed, quantum chemistry studies of finite molecules have accumulated a hierarchy of standardized optimum Gaussian basis sets.[2,3]

Since the potentials are local in real space, both the Coulomb potential and the Fock operator are more conveniently calculated in real space. This allows optimization of the computational effort to attain linear scaling with basis set size. To accomplish linear scaling we partition $\rho(\mathbf{r})$ into localized contributions, $\{\rho_a(\mathbf{r})\}$, so that the Coulomb potential can be constructed as linear superposition of local contributions. The next step is to introduce an accurate numerical grid so that construction of the Fock matrix can be done in real space. This maximizes the benefit of locality in both the Gaussian basis functions and the fields.

To accomplish this, here we develop the dual-space approach for electronic structure calculations on periodic systems using Gaussian basis functions (GDS/DFT). In GDS/DFT, projection functions are used to partition the electronic density $\rho(\mathbf{r})$ into atom-centered contributions. The Coulomb potential is then obtained by solving radial Poisson equations. The residual charges (the difference between the total density and the projected density) are then conveniently transformed to reciprocal space, where the Coulomb potential is updated. In addition, we introduce an accurate grid for calculation of the Fock matrix. Finally we develop the generalized conjugate gradient (GCG) method for updating (converging) the wave function. The advantage of GCG over standard conjugate gradients[4] (GS's) is that it avoids evaluating the total energy for every orbital update (prohibitively expensive for methods using Gaussian basis functions).

GDS/DFT has an advantage over other standard methods (plane wave,[4–6] Gaussian,[7,8] muffin tin,[9] and augmented plane waves[10–13]) in that it is applicable to all elements of the Periodic Table, and implementation of forces is straightforward. To illustrate the general appli-

cability of GDS/DFT, we report calculations for several crystals (diamond, C_{60}, AlN, GaN, and CdTe) and surfaces [GaAs(110) and Bn(110)].

The organization is as follows. Section II describes the method for calculating the Fock matrix, the design of the numerical grid, and the dual-space approach to calculating the Coulomb potential. The generalized conjugate gradient is described in Sec. III. Results of various applications are reported in Sec. IV, and a summary is in Sec. V.

II. METHOD FOR CALCULATING THE FOCK MATRIX

In GDS/DFT, the Fock matrix is calculated in real space. The Coulomb potential, exchange-correlation potential, and nuclear potential are calculated on an atom-based numerical grid, and their contributions to the Fock matrix are calculated using numerical integration. The numerical grid is divided into blocks of contiguous grid points distributed according to the symmetry of the system. Only nearby atoms make significant contributions to the fields for each grid block. Similarly, only basis functions centered on nearby atoms make significant contributions to integrating the Fock matrix in a particular grid block. With an efficient cutoff strategy, calculation of the Fock matrix in GDS/DFT scales linearly with basis set size for large systems.

The kinetic-energy contribution to the Fock matrix and the overlap matrix are calculated analytically. Although the matrix from the nuclear potential could be calculated analytically, we use numerical integration, so that this term cancels with the Coulomb potential at large distances from the atoms.

A. Numerical grid

The numerical grid in GDS/DFT is constructed by replacing three-dimensional integration of periodic functions with a set of single-center numerical integrations using properly normalized projection functions.[14] At a grid point $\mathbf{r}$ the projection function for an atom a is defined as

$$P_a(\mathbf{r})=\frac{\eta_a(\mathbf{r})}{\sum_{bR}\eta_{bR}(\mathbf{r})} , \tag{5a}$$

with

$$\sum_{aR}P_{aR}(\mathbf{r})=1 , \tag{5b}$$

where R denotes lattice vectors and a labels atoms in the central unit cell. (Clearly the projection function P_{aR} has the periodicity of the crystal.) For the projection function to be useful, it must be unity when close to atom a and must vanish when close to other atoms. We start with the Becke construction[14] for unnormalized atomic projection functions η_a:

$$\eta_a(\mathbf{r})=\prod_{b\neq a}S_3[\mu_{ab}(\mathbf{r})] . \tag{6}$$

Here the pair projection functions are given by[14]

$$S_3(\mu)=\tfrac{1}{2}[1-p_3(\mu)] , \tag{7a}$$

where

$$p_3(\mu)=p\{p[p(\mu)]\} , \tag{7b}$$

$$p(\mu)=\tfrac{3}{2}\mu-\tfrac{1}{2}\mu^3 , \tag{7c}$$

$$\mu_{ab}(\mathbf{r})=\frac{r_a-r_b}{|\tau_a-\tau_b|} , \tag{7d}$$

and r_a is the distance to the grid point $\mathbf{r}$ from atom a. The function $\mu_{ab}(\mathbf{r})$ has values between -1 and 1. It assumes the value -1 when very close to atom a and the value 1 when very close to atom b. Correspondingly $p(\mu_{ab})$, and thus $p_3(\mu_{ab})$, assumes the values -1 and 1 in these two limits. Therefore, the pair projection function $S_3(\mu_{ab})$ has values close to 1 near atom a and close to zero near atom b.

In order to ensure accuracy and stability when the atoms move, the projection functions must guarantee

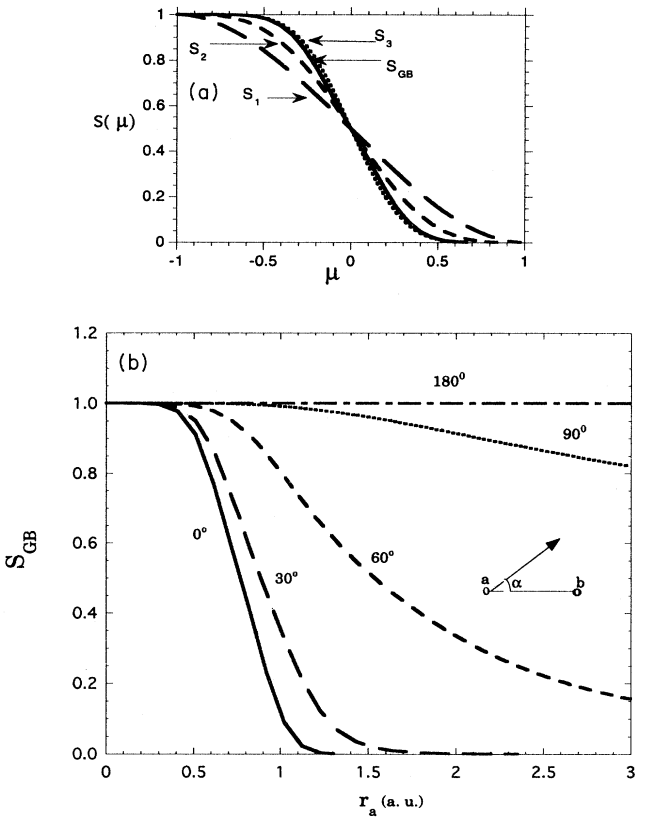

FIG. 1. (a) Comparison of the generalized Becke projection function (S_{GB}) with three constructions (S_1, S_2, and S_3) proposed by Becke (Ref. 14), plotted as a function of the diatomic coordinate μ_{ab}. All constructions approach unity at the center atom a and zero at neighboring atoms b. S_{GB} allows continuous adjustment of the projection function for different atoms. (b) The generalized Becke diatomic projection function for diamond plotted as a function of distance from atom a for five different angles: $\theta=0°$ (along the a-b bond), 30°, 60°, 90°, and 180°.

TABLE I. Numerical grids for atoms used in this paper. The first number in brackets (r_i,n_i) gives the upper boundary of the ith radial section, while the second number is the number of angular points for each radial shell in the section. r_0 is the smallest radial point. The radial grid is constructed using the geometerical scaling factor γ, Eq. (11).

Atom	(r_1,n_1)	(r_2,n_2)	(r_3,n_3)	(r_4,n_4)	(r_5,n_5)	(r_6,n_6)	(r_7,n_7)	γ	r_0
H	(0.18,12)	(0.4,26)	(0.6,50)	(3.3,194)	(12.0,116)			1.18	0.000 01
C	(0.18,12)	(0.4,26)	(0.6,50)	(3.3,194)	(12.0,116)			1.18	0.000 01
B	(0.18,12)	(0.4,26)	(0.6,50)	(3.3,194)	(12.0,116)			1.18	0.000 01
N	(0.18,12)	(0.4,26)	(0.6,50)	(3.3,194)	(12.0,116)			1.18	0.000 01
O	(0.18,12)	(0.4,26)	(0.6,50)	(3.3,194)	(12.0,116)			1.18	0.000 01
Al	(0.001,12)	(0.1,26)	(0.5,38)	(0.6,50)	(5.0,194)	(12.0,116)		1.15	0.000 001
Ga	(0.001,12)	(0.1,26)	(0.5,38)	(0.6,50)	(5.0,194)	(12.0,116)		1.15	0.000 001
As	(0.001,12)	(0.1,26)	(0.5,38)	(0.6,50)	(5.0,194)	(12.0,116)		1.15	0.000 001
Cd	(0.001,12)	(0.1,26)	(0.4,38)	(0.6,78)	(6.0,194)	(12.0,116)	(16.0,50)	1.15	0.000 001
Te	(0.001,12)	(0.1,26)	(0.4,38)	(0.6,78)	(6.0,194)	(12.0,116)	(16.0,50)	1.15	0.000 001

that two atoms decouple smoothly when far away from each other. In order to achieve the smoothest decoupling, we generalize the original Becke construction in two ways. First, we introduce a cutoff into the denominator of (7d),

$$\bar{\mu}_{ab}(\mathbf{r})\equiv\frac{r_a-r_b}{\min(R_{\text{cut}},|\tau_a-\tau_b|)}\ , \tag{8}$$

and limit the value of $\bar{\mu}_{ab}(\mathbf{r})$ to remain between -1 and 1.

Second, we introduce the generalized Becke projection function (GBPF),

$$S_{\text{GB}}(\mu)=\tfrac{1}{2}[1-p_3(\bar{\mu})]+\frac{\beta}{2}\sin[p_3(\bar{\mu})\pi]\ , \tag{9}$$

in place of Becke pair projection function (7). This modification allows the slope in the falloff region ($\bar{\mu}\sim 0$) of S_{GB} to adjust continuously in grid optimizations (see Fig. 1). The two parameters R_{cut} and β in Eqs. (8) and (9) are associated with each atom and are adjusted to optimize the accuracy of the grid. We find that $R_{\text{cut}}=5.6a_0$ (where a_0 is the Bohr radius) and $\beta=0.07$ are satisfactory for nonhydrogen atoms, while $R_{\text{cut}}=5.6$ and $\beta=0.03$ are satisfactory for hydrogen.

Because the projection function $P_{aR}(\mathbf{r})$ is periodic, the integration of a periodic function $f(\mathbf{r})$ can be decomposed into atomic integrations as in (10),

$$\int_{\text{cell}} d\mathbf{r}\, f(\mathbf{r})=\sum_a \int_{\text{atomic}} d\mathbf{r}\, P_a(\mathbf{r})f(\mathbf{r})\ . \tag{10}$$

Since the projection functions are localized, the atomic integrations in (10) are limited to atomic spheres of finite radius (between $10a_0$ and $20a_0$).

For the atomic integration we use atom-centered spherical grids constructed from concentric radial shells. Each radial shell supports an angular set of Lebedev grid points[15] that integrates exactly angular functions up to $l=17$ in the interstitial region and up to $l=5$ close to the nuclei. The radial grid is divided into several radial sections. Each section is assigned the number of angular points in Table I. Generally each radial section contains many radial shells spaced geometrically,

$$R_{i+1}=\gamma R_i\ , \tag{11a}$$

with weights given by

$$W_i=R_i^3\ln(\gamma)\ . \tag{11b}$$

We use a minimum radius of $R_0=0.000\,01a_0$, a maximum radius of $R_{\text{max}}=12.881\,62a_0$, and $\gamma=1.18$ (which

TABLE II. Numerical integration normalization error for sets of Gaussian functions.

Exponent	$l=0$	$l=1$	$l=2$	$l=3$	$l=4$
0.15	0.46×10^{-11}	0.15×10^{-9}	-0.21×10^{-9}	-0.65×10^{-8}	-0.65×10^{-8}
1.0	0.11×10^{-10}	-0.64×10^{-10}	-0.11×10^{-8}	0.78×10^{-9}	0.28×10^{-7}
5.0	0.23×10^{-11}	-0.15×10^{-9}	-0.46×10^{-9}	0.54×10^{-8}	0.20×10^{-7}
10.0	0.86×10^{-11}	-0.10×10^{-9}	-0.98×10^{-9}	0.25×10^{-8}	0.28×10^{-7}
50.0	-0.46×10^{-12}	-0.15×10^{-9}	-0.14×10^{-9}	0.62×10^{-8}	0.14×10^{-7}
100.0	0.75×10^{-11}	-0.13×10^{-9}	-0.77×10^{-9}	0.41×10^{-8}	0.25×10^{-7}
500.0	0.14×10^{-10}	-0.15×10^{-9}	0.18×10^{-9}	0.65×10^{-8}	0.73×10^{-8}
1000.0	0.55×10^{-10}	-0.15×10^{-9}	-0.50×10^{-8}	0.53×10^{-8}	0.21×10^{-7}
10 000.0	0.16×10^{-8}	-0.15×10^{-9}	-0.19×10^{-9}	0.61×10^{-8}	0.15×10^{-7}
100 000.0	0.52×10^{-7}	-0.15×10^{-9}	0.14×10^{-9}	0.65×10^{-8}	0.82×10^{-8}

TABLE III. Accuracy of molecular HF total-energy calculations using numerical integration. All energies are in mH, with 1 mH=0.027 211 6 eV=0.627 51 kcal/mol.

Molecule	Size Atoms	Size Basis	Error Total	Error per atom
Oxygen	2	30	0.004	0.002
Water	3	25	−0.007	−0.002
Carbon dioxide	5	45	−0.018	−0.006
Methane	12	35	−0.016	−0.003
Benzene	12	120	0.022	0.002
Glycine	10	100	0.024	0.002
Glutamine	20	200	0.072	0.004
Porphine	38	430	0.160	0.004
C_{60} (I_h)	60	540	0.206	0.003
C_{60} (T_h)	60	540	0.255	0.004

gives 86 radial shells). This leads to integration errors of less than 5.2×10^{-8} for Gaussian functions with exponents in the range of 0.15 to 100 000 (see Table II). Smaller γ increases the numerical accuracy at the expense of increased grid points. We tested the accuracy of this grid with analytical Hartree-Fock (HF) calculations on molecular systems. For molecular systems the construction of the grid is identical to that in crystalline systems, except that the lattice sum is absent and the projection functions are not periodic. The Fock matrix is obtained numerically for the Coulomb potential, exchange-correlation potential, and nuclear potential contributions.

The test results in Table III show that the error per atom in the total energy is less than 0.006 mH=0.16 meV, which is acceptable for studies of normal chemical processes. For C_{60} the error in the energy difference between the two structures (with I_h and T_h symmetry) is only 0.049 mH=1.33 meV.

B. Dual-space approach for construction of the Coulomb potential

The usual approach for calculating the Coulomb potential with Gaussian-type basis functions requires analytical three-center integrals. This is very expensive (the most expensive part of the self-consistent cycle) in a periodic system because of the slow convergence in the lattice sum. We overcome this problem by taking advantage of the different convergence properties for the core and valence electrons in real and reciprocal spaces. The idea is to project the total density into atom-centered pieces which are used to calculate their contributions to the Coulomb potential in real space. The residual charge density (difference between the total density and the projected density) is mainly in interstitial regions whose contribution to the Coulomb potential can be calculated easily in reciprocal space.

The projection works in the following way. From (5b) we have

$$\rho(\mathbf{r})=\sum_a\sum_R P_{aR}(\mathbf{r})\rho(\mathbf{r})\equiv\sum_{aR}\rho_{aR}(\mathbf{r}) \ . \tag{12a}$$

where the projected density ρ_{aR} is both localized and periodic. Consider an atom a in the unit cell (all coordinates are then referenced to atom a). The Coulomb potential from each locally projected charge density is obtained by solving the atom-centered Poisson equation [see (15) below]. We first express ρ_a as a partial-wave decomposition in terms of cubic harmonics X_{lm},

$$\rho_a(\mathbf{r})=\sum_{lm}^{l_{\max}}\rho_{lma}(r)X_{lm}(\Omega_a) \ , \tag{12b}$$

where the limits on m are $-l$ to $+l$ and the limits on l are 0 to $l_{\max}$. We next introduce the screened density $\bar{\rho}$, which for each angular momentum about atom a is expressed in terms of two Gaussian functions according to

$$\bar{\rho}_{lma}(r)=(c_{lma}e^{-Z_1r^2}+d_{lma}e^{-Z_2r^2})r^l \ . \tag{13a}$$

Here we choose

$$Z_2=1.4Z_1 \ . \tag{13b}$$

The value of Z_1 is somewhat arbitrary. We find it convenient to choose small Z_1 for systems with large unit-cell volume in order to limit costs of reciprocal-space calculations. A value of Z_1 between 0.3 and 1.0 was found to be appropriate for the applications reported here. The two parameters c_{lma} and d_{lma} in (13) are determined to satisfy the screening conditions

$$\int r^2dr\,\rho_{lma}(r)=\int r^2dr\,\bar{\rho}_{lma}(r) \ , \tag{14a}$$

and

$$\int r^2dr\,\rho_{lma}(r)r^l=\int r^2dr\,\bar{\rho}_{lma}(r)r^l \ . \tag{14b}$$

Equations (13) and (14) ensure that the moments satisfy

$$M^p=\int r^{p+2}dr(\rho_{lma}-\bar{\rho}_{lma})\times\int d\Omega\,P_p(\Omega)X_{lm}(\Omega)=0 \tag{14c}$$

for $p\le l$ [where $P_p(\Omega)$ is the Legendre polynomial of order p]. [For $l=0$ we use only a simple Gaussian function in (13a) with the parameter determined by (14a)]. This screening ensures a zero Coulomb potential outside the range of the atomic grid. The screening charges are taken into account in reciprocal space in the spirit of the Ewald method.

The Coulomb potential is calculated easily by solving the radial Poisson equation[66]

$$\left[\frac{d^2}{dr^2}-\frac{l(l+1)}{r^2}\right]U_{lm}(r)=-4\pi r\rho_{lm}(r) \tag{15}$$

over a discrete radial grid. The derivatives are evaluated using the seven-point Lagrange formula (except for boundary points where we use four, five, and six points to ensure a banded matrix). Thus the Poisson equation (15) transforms to linear algebraic equations having a banded matrix on the left-hand side.

The Coulomb potential of the crystal then becomes

$$V(\mathbf{r})=\sum_R\sum_a\sum_{lm}^{l_{\max}}U_{lma}(r_{aR})X_{lm}(\Omega_{aR})/r_a \ , \tag{16}$$

where the sum is over all lattice vectors R, and subscript aR indicates that all coordinates are referenced to atom

aR. Since the Poisson equation is solved in the atomic grid, we use cubic splines to interpolate $U_{lma}(r)$ from the atomic grid to the crystal grid.

The residual charge

$$\rho_{\rm res}(\mathbf{r})=\rho(\mathbf{r})-\sum_{aR}\sum_{lm}^{l_{\max}}\rho_{lmaR}(r_{aR})X_{lm}(\Omega_{aR}) \tag{17}$$

is Fourier transformed to reciprocal space (see the Appendix for technical details) to update the corrections in the Coulomb potential. With this correction, the dual-space approach is exact, while having the benefit of fast convergence in reciprocal space and efficiency in real space. The computational cost in real space is linear in size and negligible for all applications reported in this paper (we use an angular momentum cutoff of $l_{\max}=3$).

Recently Termath and Handy[8] reported a study on small molecules using the Becke numerical grid. They concluded that analytical evaluation of the Coulomb potential is faster than solving Poisson equations, where they find that cubic spline interpolation dominates the computational costs. This is a surprising conclusion since the interpolation need be done only for the radial grid. Our test on crystals indicates that the numerical approach is faster by almost two orders of magnitude than the analytical approach. The discrepancy between our results and theirs might be because (1) they used the maximum angular grid throughout the space (this is unnecessary waste) which would contribute to the expense due to the rapidly growing number of spherical harmonics as angular momentum increases; (2) we use a projection function in our approach which reduces the number of centers to the number of atoms in the unit cell (normally for a crystal there are a large number of centers contributing to the Coulomb potential); (3) we use a dual-space approach, allowing us to limit the cost in real space by using small angular momentum cutoff; and (4) we use an efficient grid which also contributes to the savings in computational cost for our method.

Once the Coulomb potential is calculated on the grid, the exchange-correlation potential, Coulomb potential, and nuclear potential are combined together to obtain the Fock matrix elements numerically using (10). The nuclear-nuclear interaction energies are calculated using standard Ewald methods.[17] For systems with fcc, bcc, and hcp symmetries, the sampling of the Brillouin zone is done using standard special k points.[18] For other less symmetric systems, we use the Froyen[19] method with the number of irreducible k points minimized by adjusting the parameter f_0 in Eq. (3) of Ref. 19.

C. Calculation of total energy and forces

The calculation of forces in GDS/DFT is facilitated by the use of an optimized numerical grid. The ground-state energy is given by

$$E_{\rm tot}=E_{\rm kin}+E_{\rm xc}+E_{\rm elect} \tag{18a}$$

$$E_{\rm elect}=E_{\rm ee}+E_{\rm en}+E_{\rm nn}\ , \tag{18b}$$

where $E_{\rm kin}$ is the kinetic energy, $E_{\rm xc}$ is the electronic exchange-correlation energy, $E_{\rm ee}$ is the Coulomb interaction energy between electrons, $E_{\rm en}$ contains all interactions between electrons and nuclei (for heavy atoms this is modeled by a pseudopotential PP), and $E_{\rm nn}$ contains all the nuclei-nuclei interactions (including any residual interactions between the PP for heavy atoms).

The calculation of $E_{\rm kin}$ is done analytically using the Obara and Saika[16] recursion relation. $E_{\rm xc}$ is calculated easily using the numerical grid. The $E_{\rm elect}$ terms take more care. For convenience we introduce square brackets to represent Coulomb-type integrals. Thus $E_{\rm nn}=\frac{1}{2}[\rho_n\|\rho_n]$, $E_{\rm en}=[\rho_e\|\rho_n]$, and $E_{\rm ee}=\frac{1}{2}[\rho_e\|\rho_e]$, where ρ_n and ρ_e, respectively, are nuclei charges (point charges in the case of all-electron calculations and Gaussian functions in the case of pseudopotential calculations).

In GDS/DFT electrons and nuclei are screened separately to accelerate convergence of Ewald sums. Thus we have

$$E_{\rm elect}=E_{\rm lat}+E_{es}\ , \tag{19a}$$

where

$$E_{\rm lat}=\tfrac{1}{2}[\rho_n\|\rho_n-\rho_w]+\tfrac{1}{2}[\rho_n\|\rho_w]-\tfrac{1}{2}[\rho_s\|\rho_s] \tag{19b}$$

and

$$E_{es}=\tfrac{1}{2}[\rho_e+\rho_s\|\rho_e+\rho_s]+[\rho_e\|\rho_n-\rho_s]\ , \tag{19c}$$

where ρ_w is the screening charge for nuclei and ρ_s is the screening charge for electrons. Both screening charges are s-type Gaussian functions with the exponent of ρ_s twice that of ρ_w. With this choice the last two terms in (19b) cancel out, leading to

$$E_{\rm lat}=\tfrac{1}{2}[\rho_n\|\rho_n-\rho_w]\ . \tag{19b'}$$

The calculation of $[\rho_n\|\rho_n-\rho_w]$ is done easily with standard analytical approaches (involving a lattice sum of complementary error functions).[17]

The calculation of the E_{es} involves first obtaining the potentials $V_c(r)=\langle r|\rho_e+\rho_s]$ and $V_{ns}(r)=\langle r|\rho_n-\rho_s]$ using the dual-space approach described in Sec. II B. Then the calculation of energy is carried out via straightforward numerical integration on the grid.

The calculation of forces follows the same procedure. The only special point is the contribution from $E_{cs}=\frac{1}{2}[\rho_e+\rho_s\|\rho_s+\rho_s]$. The force coming from this term is given by

$$F_{cs}^{a}=\int d\mathbf{r}\frac{d[\rho_e(\mathbf{r})+\rho_s(\mathbf{r})]}{da}V_c(\mathbf{r})\ ,$$

where a indicates an atomic coordinate. Thus the only significant extra cost in calculating the force is the evaluation of the density gradient, which can be done simultaneously with an evaluation of the density. Similarly for the force resulting from $[\rho_e\|\rho_n-\rho_s]$, we have

$$F_{ns}^{a}=\int d\mathbf{r}\frac{d[\rho_e(\mathbf{r})]}{da}V_{ns}(\mathbf{r})+\int d\mathbf{r}\,\rho_e(\mathbf{r})\frac{dV_{ns}(\mathbf{r})}{da}\ ,$$

where the gradient of V_{ns} can be done analytically.

III. WAVE-FUNCTION UPDATE USING GENERALIZED CONJUGATE GRADIENTS

With the dual-space approach of Sec. II B, the wave-function update becomes the dominant computational step for self-consistent calculations of large systems. For plane-wave pseudopotential (PW-PP) calculations, much progress has been made in the application of conjugate gradient (CG) methods.[20] The basic steps in CG's are as follows.

(1) Find the gradient vector $|g_n\rangle$ for an orbital $|\psi_n\rangle$:

$$|g_n\rangle = -(F-\epsilon_n)|\psi_n\rangle \ , \tag{20a}$$

where F is the Fock matrix and ϵ_n the orbital eigenvalue.

(2) Construct the conjugate vector $|h_n\rangle$:

$$|h_n\rangle = |g_n\rangle + \gamma_n |h_n'\rangle \ , \tag{20b}$$

where $|h_n'\rangle$ is the conjugate vector from the previous iteration,

$$\gamma_n = \frac{\langle g_n|g_n\rangle}{\langle g_n'|g_n'\rangle}$$

and $|g_n'\rangle$ is the gradient vector from the previous iteration.

(3) Orthogonalize $|h_n\rangle$ to $|\psi_n\rangle$ and to $|\psi_p\rangle$, where $p<n$.

(4) Update the wave function as

$$|\psi_n^{\rm new}\rangle = |\psi_n\rangle\cos(\theta) + |h_n\rangle\sin(\theta) \ , \tag{21}$$

where the rotation angle θ is obtained by energy minimization (the orthonormalized vectors $|\psi_n\rangle$ and $|h_n\rangle$ are mutually orthogonal).

Step (4) dominates the computational cost. The energy minimization requires the first derivative

$$\left[\frac{\partial E}{\partial\theta}\right]_{\theta=0} = 2\,{\rm Re}\{\langle h_n|F|\psi_n\rangle\} \tag{22}$$

and the second derivative

$$\left[\frac{\partial^2 E}{\partial\theta^2}\right]_{\theta=0} = \langle h_n|F|h_n\rangle - \langle\psi_n|F|\psi_n\rangle + \eta_n \tag{23}$$

(or another quantity of equivalent cost). The first derivative and the first two terms in (23) are obtained easily from the Fock matrix. The most expensive part is

$$\eta_n = 2\,{\rm Re}\left\{\langle h_n|\left[\frac{\partial V_{\rm coul}(r)}{\partial\theta}+\frac{\partial V_{\rm xc}(r)}{\partial\theta}\right]|\psi_n\rangle\right\} \ , \tag{24a}$$

which would involve an effort equivalent to one evaluation of the Fock matrix for each occupied orbital. This is unacceptable. Since η_n is generally small, we use the following empirical expression:

$$\eta_n = f\sum_j^{\rm unocc}\frac{|\langle h_n|F|\psi_j\rangle|^2}{\langle h_n|F|h_n\rangle-\epsilon_n} \tag{24b}$$

where the constant f is introduced to account for the approximate nature of η_n. We have found $f=1$ to be satisfactory for applications considered herein. Smaller f results in faster convergence but can sometimes cause convergence instabilities, especially for poor initial guesses. Large f causes slower convergence.

In addition to the above modification for line minimization (21), we also use a preconditioning of the gradient so that it becomes parallel to the direction obtained by a second-order method. For calculations with plane waves this is difficult to achieve, and only the diagonal kinetic contribution is preconditioned.[20] For calculations with Gaussians, this is done easily using the preconditioning operator

$$\sum_j^{\rm occ}\frac{|\bar\psi_j\rangle\langle\bar\psi_j|}{\sqrt{(\epsilon_n-\epsilon_j)^2+\omega^2}} \tag{25}$$

where $\bar\psi_j$ is the jth eigenfunction of the Fock matrix, and ω is the energy scale over which orbital mixing occurs. The scale of ω is the order of the gap, $\epsilon_{\rm gap}$, at the beginning of the self-consistent loop, and decreases as convergence is achieved. Empirically we find the following expression for ω to be satisfactory:

$$\omega^2 = \kappa\epsilon_{\rm gap}\sqrt{|\langle g_n|h_n\rangle|} \ , \tag{26}$$

with $\kappa=1$. This has the property that closes to convergence

$$\omega^2 \sim \kappa\epsilon_{\rm gap}\sqrt{(\langle\psi_n|F^2|\psi_n\rangle-\epsilon_n^2)} \ .$$

Tables IV and V report convergence tests for a number of molecules and crystals. Comparing to the direct inversion in the iterative subspace (DIIS) method[21] (the

TABLE IV. Number of iterations to achieve convergence of 10^{-5} for Hartree-Fock (HF) and GDS/DFT using GCG.

Molecule	N_2	O_2	H_2O	CH_4	C_6H_6	glycine	glutamine	$C_{60}I_h$	$C_{60}T_h$
$N_{\rm basis}$[a]	30	30	25	35	120	100	200	540	540
$N_{\rm occ}$[b]	7	8	5	5	21	20	39	180	180
HF (DIIS)	6	6	7	7	8	9	0	8	9
GDS/DFT (GCG)	5	6	9	7	8	12	15	10	9

[a] $N_{\rm basis}$ is the number of basis functions.

[b] $N_{\rm occ}$ is the number of occupied molecular orbitals.

TABLE V. Number of iterations to achieve convergence of 10^{-5} for GDS/DFT calculations of crystalline sytems. Notation as in Table IV.

Method	Diamond	c-BN	h-BN	c-AlN	c-GaN	GaAs	CdTe	C_{60}
N_{basis}	30	30	60	34	50	70	78	540
N_{occ}	6	6	12	10	19	32	50	180
GDS/DFT (GCG)	8	8	8	9	12	15	15	11

current method of choice for *ab initio* Hartree-Fock calculations in molecular systems) GCG requires much less memory. Thus DIIS requires storing the full Fock matrices in previous steps, leading to a size of

$$N_{DIIS}=N_{iter}\tfrac{1}{2}N_{basis}^2 , \tag{27a}$$

while GCG requires only the immediate precedent conjugate vectors and wave functions, leading to

$$N_{GCG}=N_{occ}N_{basis}+(\tfrac{1}{2})N_{basis}^2 . \tag{27b}$$

Also GCG converges well for both molecular systems and for solids.

IV. APPLICATIONS

A. Diamond

Diamond is the prototypical covalently bonded insulator with highly directional sp^3 bonding. Each carbon atom in diamond is bonded tetragonally to its four nearest neighbors, forming a close-packed fcc structure with two atoms per unit cell. It leads to large deviations from overlapping spherical densities and provides a good test case for real-space approaches. Diamond leads to a hard-core pseudopotential, requiring large basis sets for PW-PP calculations.

We used the Dunning-Huzinaga basis set,[3] which is the standard for *ab initio* calculations of first-row elements. This basis set consists of ten primitive *s*-type Gaussians contracted into three basis functions (the grouping is 7-2-1) and five primitive *p*-type Gaussians contracted into two basis functions (the grouping is 4-1) for each of the three components. To account for polarization effects in the valence orbitals, we add one set (six) of *d*-type Gaussians with exponent 0.75. This basis set is denoted DV^*. Using the Pople 6-31G basis set[3] augmented with one *d* function (631-G^*) gives no appreciable difference in band structure (the maximum difference is 0.04 eV) for the conduction band and 0.07 eV for the valence band).

To facilitate comparison with other band-structure calculations, the experimental lattice constant $a=3.567$ Å was used, and the self-consistent potential was obtained using ten special k points[18] in the irreducible wedge of the fcc Brillouin zone. The atomic grid (constructed according to Sec. II) has 317 inequivalent points in the irreducible wedge. The Hedin-Lundquist form for the exchange-correlation potential[22] was used.

The lattice constant and bulk modulus are reported in Table VI. The lattice constant is 0.032 Å smaller than experiment and 0.005 Å larger than PW-PP. The calculated band structure is reported in Table VII (and Fig. 2). We obtain a band gap of 4.04 eV, in good agreement with PW-PP results[28] (4.05 eV) and about 30% smaller than the experimental value of 5.47 eV.[26] This large discrepancy is due to the LDA, which fails to reproduce the discontinuity of the exchange correlation potential across the Fermi surface.[29]

TABLE VI. Lattice constant (a) and bulk modulus (B) for diamond.

	Expt.[a]	GDS/DFT	PW-PP[b]	PP-GTO[c]	PP-LCAO[d]
a (Å)	3.567	3.535	3.530	3.69	3.56
B (Mbar)	4.52	4.57	4.73	4.56	4.37

[a]Reference 26.
[b]Plane-wave pseudopotential, Ref. 23.
[c]Pseudopotential linear combination of Gaussian basis functions, Ref. 24.
[d]Pseudopotential linear combination of atomic orbitals, Ref. 25.

B. GaAs(110) surface

GaAs(110) is one of the most studied semiconductor surfaces. Generalized valence bond (GVB) calculations show that the two dangling bonds broken at the surface coalesce into one lone pair of electrons localized on the As center.[30] This surface is therefore a good test case for LDA-type calculations since spin polarizations are not required. The cleaved GaAs(110) surface has the same

TABLE VII. Energy levels for diamond.

	GDS/DFT	LCAO[a]	LAPW[b]	PW-PP[c]
Γ_1	−21.35	−21.34	−21.06	−21.38
$\Gamma_{25'}$	0.00	0.00	0.00	0.00
$\Gamma_{15'}$	5.53	5.57	5.51	5.51
$\Gamma_{2'}$	13.55	13.56	13.13	13.56
X_1	−12.64	−12.66	−12.48	−12.67
X_4	−6.30	−6.34	−6.18	−6.31
X_1	4.70	4.79	4.68	4.64
X_4	16.60	16.71	16.41	16.81
$L_{2'}$	−15.51	−15.52	−15.33	−15.53
L_1	−13.38	−13.41	−13.14	−13.47
$L_{3'}$	−2.82	−2.81	−2.73	−2.81
L_3	8.36	8.45	8.33	8.37
L_1	9.01	9.07	8.75	8.97

[a]Linear combination of atomic orbitals, Ref. 7.
[b]Linear augmented plane waves, Ref. 27.
[c]Plane wave pseudopotential, Ref. 28.

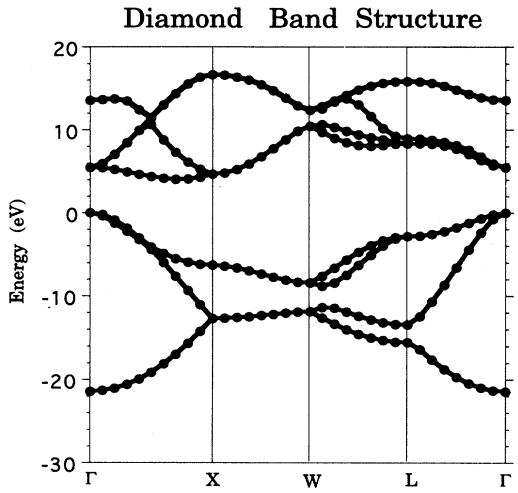

FIG. 2. The band structure of diamond calculated with GDS/DFT (DV^* basis) at the experimental lattice constant ($a=3.567$ Å).

stoichiometry as the bulk, and it relaxes without significant reconstruction.[31] The hybridization angle of the unrelaxed surface, 109.5°, changes toward the ideal hybridization angles (120° for Ga and 94.3° for As) (Ref. 32) as it relaxes. This causes the surface As atom to move away from the bulk while the Ga atom moves down into the surface, roughly preserving the bond lengths.[31]

For these calculations we use the *ab initio* $MS4$ basis set[33] with additional valence d functions optimized from calculations of GaAs crystal (exponents of 0.286 for Ga and 0.396 for As). The $MS4$ basis is contracted as (43321/4321/311) for both Ga and As to form a split valence basis ($1s,2s,3s,4s,4s'$; $2p,3p,4p,4p'$; and $3d,3d',4d$) where the outer d Gaussians ($4d$) describes valence polarization effects.

We used ten special k points[18] to sample the irreducible Brillouin zone and the Ceperley-Alder exchange-correlation potential as parametrized by Perdew and Zunger.[34] We obtain a bulk lattice constant $a=5.678$ Å, in good agreement with the experiment ($a=5.65$ Å) (Ref. 35) but 0.13 Å larger than the PW-PP result ($a=5.52$ Å).[36] It is not known why PW-PP leads to such a small cell;[36,37] it may result from the significant overlap between the shallow Ga $3d$ electrons and the valence charge density.

The surface calculations were carried out using a periodic slab (see Fig. 3) of three double layers (total thickness $\simeq 12$ Å) separated by a vacuum of two double layers (thickness $\simeq 8$ Å). The irreducible Brillouin zone was sampled using eight special k points optimized with the Froyen[37] method (see also Sec. III about our modifications). In these calculations we fixed the Ga—As bond lengths at the theoretical bulk value and allowed only the surface atoms to relax. This leads to a single degree of freedom, the angle ω between the surface Ga—As bond and the [001] direction (the reconstruction angle). This rigid-bond-first-layer only approximation captures the dominant effects of surface relaxation (fully relaxed

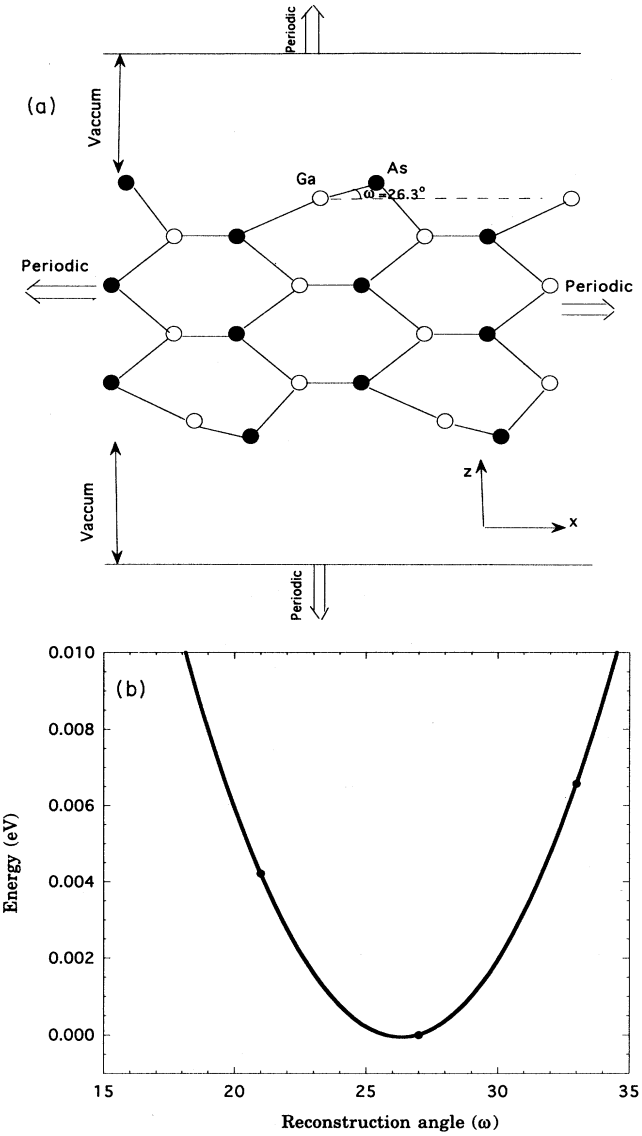

FIG. 3. (a) Side view of the relaxed GaAs(110) surface ($\omega=26.3°$). (b) Potential curve for relaxation using GDS/DFT ($MS4^*$ basis).

ab initio calculations[38] lead to relaxations in the lower layers that are an order of magnitude smaller). The results are summarized in Table VIII. We obtain $\omega=26.3°$, which agrees reasonably well with other theoretical calculations[36] ($\omega=27.4°-31.6°$). It is quite close to the GVB cluster calculations ($\omega=25.8°$).[30] The LEED data lead to $\omega=28.0°$ obtained by Tong, Mei, and Xu[39] and $\omega=31.1°$ obtained by Duke *et al.*[40] We find the average As—Ga—As bond angle to be 119.3° [slightly smaller than the ideal angle (120°) for trivalent Ga] and the average Ga—As—Ga bond angle to be 96.5° [somewhat larger than the ideal angle of 94.3° (for AsH_3)]. These results agree very well with GVB cluster calculations,[30] which give average angles of 119.3° for Ga and 95.8° for As.

TABLE VIII. Reconstruction of GaAs(110) surface. Reported in the table are the bulk lattice constants.

	Experiment[a]	GDS/DFT	PW-PP[b]
a (Å)[c]	5.65	5.678	5.52
ω (degree)[d]	27.0,31.3	26.4	27.0,28.5
Asδz (Å)[e]	0.09,0.19	0.19	0.19,0.22
Gaδz (Å)[e]	−0.506,−0.527	−0.446	−0.44,−0.51
d_{12} (Å)[f]	0.65,0.75	0.63	0.58∼0.68

[a]Experimental data, summarized in Ref. 36.
[b]Plane-wave pseudopotential calculations, summarized in Ref. 36.
[c]Bulk lattice constant for three-dimensional crystal.
[d]Reconstruction twist angle.
[e]Displacements of surface atoms perpendicular to the surface.
[f]The difference of the two surface displacements (most sensitive quantity from LEED experiments).

C. BN(110) surface

Cubic boron nitride is of considerable interest because of its hardness and possible use as substrate material for CVD growth of diamond films.[41] BN is also interesting as an adherent coating of ceramics such as MgO.[42] However, there is very little experimental data available on the electronic structure for the cubic (zinc blende) form of BN, and few theoretical or experimental studies of BN surfaces.

Our calculations use the *ab initio MS*4 basis set[33] with additional valence d functions optimized for cubic BN (exponents of 0.337 for B and 0.7994 for N). The bulk calculation used the Ceperley-Alder–Perdew-Zunger exchange-correlation potential[34] and two special k points[18] to sample the irreducible Brillouin zone. We obtain a lattice constant $a=3.593$ Å, very close to the experimental value of 3.615 Å (Ref. 43) and to PW-PP calculations (3.606 Å).[44] We find a bulk modulus of $B=3.764$ Mbar, slightly larger than the PW-PP result[44] (3.67 Mbar). These values are significantly lower than estimated value of 4.65 Mbar reported in Ref. 44 using an empirical interpolation of experimental elastic constants.[45] This estimated experimental value is larger than the bulk modulus for diamond (4.52 Mbar) and is, we believe, too large.

We examined the (110) surface for cubic BN using a slab of four double layers separated by a vacuum with a thickness corresponding to two double layers. The irreducible Brillouin zone was sampled using two special k points constructed as for GaAs. As for GaAs, we used the rigid-bond-top-layer only approximation. We obtain a reconstruction angle of $\omega=15.58°$, corresponding to average hybridization angles of 116.37° for the cation and 99.03° for the anion. Similar calculations using two double layers with six k points ($\omega=15.26°$) and two double layers with two k points ($\omega=15.44°$) give no significant difference in structural properties. This is smaller than the $\omega=21.7°$ from Hartree-Fock cluster calculations[46] (where the hybridization angles for B and N are found to be 118.7° and 103.5°, respectively). This difference might be due to the use of the cluster approximation or the lack of d basis functions for boron in Ref. 46. We could find no experimental data for comparison.

D. C_{60} crystal

The fullerite allotrope of carbon, C_{60}, has been of considerable interest because of possible chemical and biological applications and because of the superconductivity at 33 K in its alkali-doped compounds. The use of Gaussian basis sets has an advantage here since all electronic properties are directly expressed in terms of local orbitals. This facilitates a tight-binding interpretation and is useful for extracting parameters for model studies of superconducting mechanism.

Below 249 K, the C_{60} molecules are rotationally ordered[47] and the crystal structure has a simple cubic lattice with four C_{60} molecules per unit cell. At high temperatures the C_{60} molecules rotate freely around their center, leading to a strictly fcc structure. For computational convenience, all calculations were performed using a hypothetical fcc structure having a single C_{60} molecule per cell oriented according to the cubic symmetry. This approximation reduces the C_{60} center from I_h symmetry to T_h symmetry. The distortion caused by this symmetry reduction is very small.[48]

The structure of I_h C_{60} can be described by two parameters, namely the short carbon-carbon bond distance R_1 and the long C—C bond R_2. Our calculations used $R_1=1.414$ Å and $R_2=1.455$ Å obtained from molecular mechanics simulations.[49] We used the 6-31G basis set,[3] giving to a total 540 basis functions per unit cell. The Brillouin-zone sampling was done with one special k point. Tests using two special k points give energy differences of less than 0.01 eV in the valence and conduction bands.

The band structure in Fig. 4 shows C_{60} to be a direct-gap insulator with $E_{gap}=0.97$ eV at the X point. This is

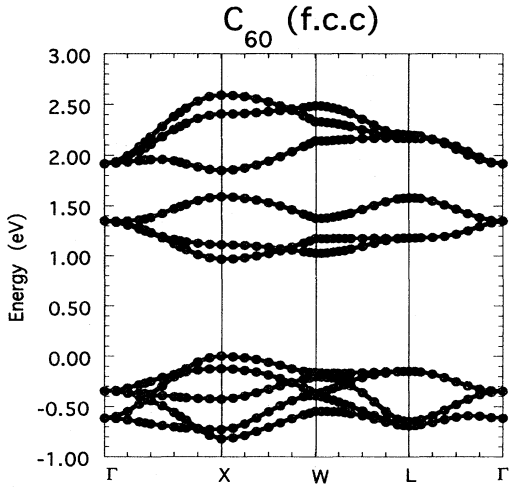

FIG. 4. Band structure of fcc C_{60} at $a=14$ Å using GDS/DFT (DV^* basis).

TABLE IX. Key parameters in the band structure of face-centered-cubic C_{60} obtained by calculating the Coulomb potential either analytically or numerically. All quantities are in eV.

	Analytical	Numerical
Band gap	0.96	0.97
W_{T1u}[a]	0.62	0.60
W_{Hu}[b]	0.84	0.83
W_{T1g}[a]	0.74	0.71

[a]Bandwidths of the two lower conduction bands.
[b]Bandwidth of the top valence band.

slightly smaller than PW-PP result ($E_{gap}=1.04$ eV),[50] presumably due to the use of different structural constants. To check the numerical accuracy in our calculations, we carried out a parallel calculation where the Coulomb potential is calculated analytically. The numerical errors are found to be less than 0.02 eV (see Table IX). To check the basis set error, we carried out a parallel calculation using the Dunning-Hunzinaga basis set[2,3] The results agree with the 6-31G results within 0.07 eV in the energy range between -21.42 and 16.62 eV.

Both theoretical results are much smaller than the experimental gap of $E_{gap}=1.85$ eV from microwave conductivity experiments[51] and the values of $E_{gap}=2.3-2.6$ eV from photoemission experiments.[52,53] It is expected that LDA calculations lead to too small a gap.

E. GaN and AlN materials

The group-III nitrides (GaN, AlN) are attracting considerable interest because of their particular stability at high temperatures, considerable hardness, and potential device applications due to the wide band gap.[54] The nitrogen favors formation of short bonds, leading to a wurtzite crystal structure with small c/a axial ratio [1,600 for AlN (Ref. 55) and 1.628 (Ref. 56) for GaN]. The energy differences between the wurtzite form and zinc-blende form are very small, and GaN zinc-blende films have grown on a single-crystalline GaN buffer which is epitaxially grown at low temperature on Si(001) by electron cyclotron resonance microwave-plasma-assisted molecular-beam epitaxy.[54] Because of the large ionicity, high pressures transform the wurtzite structure in these systems into the rocksalt structure (AlN at 12.9 GPa and GaN at 47 GPa) rather than into the zinc-blende structure.[57]

Experimental data on the microscopic parameters and electronic properties are scarce due to the difficulties in growing high quality single crystals. Recently there have been several theoretical studies. In muffin-tin-based methods, the large ionicity and directional bonding in nitrides make the atomic sphere approximation quite unreasonable. Full potential linear muffin-tin orbital (FP-LMTO) and full potential linear augmented plane-wave (FP-LAPW) methods should overcome this difficulty, but it is not clear whether they are sufficiently accurate to resolve the small energy differences between different phases and to provide a correct transition pressure.

Here we present Gaussian-based DFT calculations for the zinc-blende structure of GaN and AlN using two special k points[18] to sample the irreducible Brillouin zone. The calculations were carried out using the $MS4$ basis set[33] with an additional set of d functions (optimized exponents of 0.88 for N, 0.2378 for Al, and 0.286 for Ga). The omission of these polarization d functions leads to a slight increase in the lattice constant (by 0.3% for AlN, 0.03% for GaN) and significantly increases the bulk modulus (by 32% for AlN and 4.4% for GaN).

For AlN (see Table X), we obtain a lattice constant of 4.395 Å (4.408 Å without d functions), in close agreement with the experimental value [4.37 Å (quoted in Ref. 58)] and with PW-PP calculations [4.35 Å (Ref. 37)]. We find the bulk modulus to be 1.71 Mbar (2.26 Mbar without d functions). *Ab initio* Hartree-Fock gives 2.25 Mbar,[59] while LMTO calculations[58] give 2.15 Mbar. The experimental result quoted in Ref. 44 is 2.06 Mbar.

The band structure is presented in Fig. 5. We find zinc-blende AlN to have an indirect minimum band gap ($\Gamma_1^v \rightarrow X_1^3$) of 3.08 eV (3.14 eV for calculations without d functions). This is in close agreement with the PW-PP result (3.2 eV).[37] Both theoretical results lead to a much smaller gap than experiment (6.2 eV from optical-absorption data[60]). We calculate a direct gap at the Γ point ($\Gamma_1^v \rightarrow \Gamma_1^c$) of 3.96 eV (3.89 eV without d functions), somewhat smaller than 4.2 eV obtained with PW-PP.[37] As discussed above, the LDA is expected to underestimate the band gap.[29]

For GaN (see Table XI), we obtain a lattice constant to be 450 Å (4.52 Å without d functions). The results are in close agreement with experimental data [4.50 Å (Ref.

TABLE X. Properties of cubic AlN.

	GDS/DFT with d	GDS/DFT no d	Expt.[a]	FP-LMTO[b]	PW-PP[c]	HF[d]
Lattice constant (Å)	4.395	4.408	4.37	4.334	4.35	4.287
Bulk modulus (Mbar)	1.709	2.264	2.06	2.15		2.25
Indirect gap ($\Gamma_1^v \rightarrow X_1^c$)	3.08	3.14	6.2		3.2	
Direct gap ($\Gamma_1^v \rightarrow \Gamma_1^c$)	3.96	3.89			4.2	

[a]Quoted in Ref. 58.
[b]Full potential linear muffin-tin orbital method, Ref. 58.
[c]Plane-wave pseudopotential method, Ref. 37.
[d]*Ab initio* Hartree-Fock, Ref. 59.

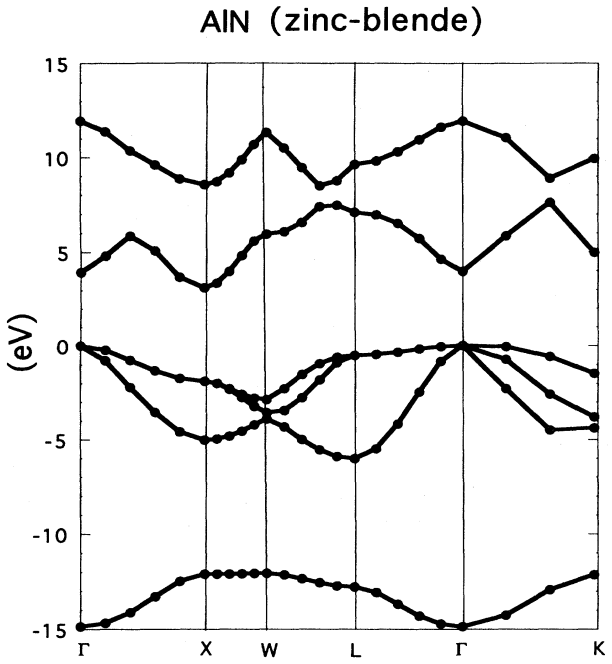

FIG. 5. Band structure of zinc-blende AlN at the theoretical lattice constant ($a=4.395$ Å) using GDS/DFT with the $MS4^*$ basis.

54)] and with PW-PP calculations (4.42 Å).[61] We find a bulk modulus of 1.58 Mbar (1.65 without d functions). We could not find other reports of this property either from theory or experiments. However, experimental data for the wurtzite form lead to $B=1.95$ Mbar, somewhat higher than the calculated zinc-blende bulk modulus.

Band-structure calculations (see Fig. 6) indicate that GaN has a direct minimum gap of 2.00 eV (1.96 eV for calculations without d functions) at the Γ point ($\Gamma_6^v \rightarrow \Gamma_1^c$). This is in close agreement with the PW-PP result of 2.1 eV but substantially smaller than the experimental value of 3.5 eV.[60] We calculate an indirect gap ($\Gamma_{15}^v \rightarrow X_1^c$) of 3.26 eV (3.04 eV for calculations without d functions), again close to the PW-PP result of 3.2 eV in PW-PP.

TABLE XI. Properties of cubic GaN. Same notation as for Table X.

	GDS/DFT with d	GDS/DFT no d	Experiment	PW-PP[a]
Lattice constant (Å)	4.50	4.52	4.50[b]	4.42[c]
Bulk modulus (Mbar)	1.58	1.65		
Indirect gap ($\Gamma_6^v \rightarrow \Gamma_1^c$)	2.00	1.96	3.2[a]	2.1[a]
Direct gap ($\Gamma_{15}^v \rightarrow X_1^c$)	3.26	3.04		3.2[a]

[a]Reference 60.
[b]Reference 54.
[c]References 61.

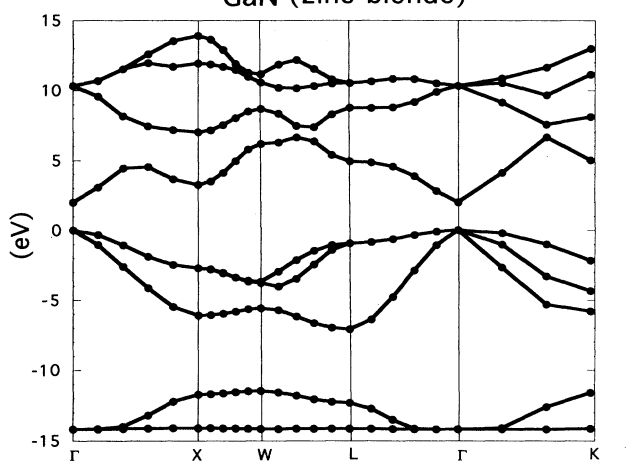

FIG. 6. Band-structure zinc-blende GaN at the theoretical lattice constant ($a=4.50$ Å) using GDS/DFT with the $MS4^*$ basis.

F. CdTe band structure

II-VI semiconductors, such as CdTe, are of current interest because of potential device applications.[62] We use the $MS4$ basis set augmented with an additional set of d-type polarization functions (exponents of 0.5889 for Cd and 1.023 for Te). We use the Hedin-Lundquist exchange-correlation potential and two special k points[18] to sample the irreducible Brillouin zone. We find a lattice constant of 6.478 Å, in good agreement with the experimental value of 6.48 Å,[60] but smaller than the LAPW

TABLE XII. Band structure of CdTe calculated at the theoretical lattice constant (6.4778 Å).

	LAPW[a]	GDSP/DFT[b]	GDS/DFT
Relativistic	Yes	Yes	No
Γ_{1v}	−11.30	−11.21	−10.32
Γ_{15d}	−8.43	−8.20	−8.24
Γ_{12d}	−8.17	−7.97	−7.66
Γ_{15v}	−0.00	−0.00	−0.00
Γ_{1c} (gap)	0.47	0.58	1.72
Γ_{15c}	4.48	4.53	4.82
Γ_{15d}	−8.43	−8.20	−8.24
χ_{1v}	−10.79	−10.67	−9.84
χ_{3v}	−4.44	−4.42	−4.11
χ_{5v}	−1.92	−1.91	−1.93
χ_{1c}	2.45	2.44	2.68
χ_{3c}	2.54	2.67	3.41
L_{1v}	−10.91	−10.80	−9.92
L_{1v}	−4.54	−4.55	−4.37
L_{3v}	−0.80	−0.79	−0.79
L_{1c}	1.60	1.66	2.54

[a]Reference 63.
[b]Reference 60, using relativistic BHS pseudopotentials from Ref. 65 in the separable form described in Ref. 64.

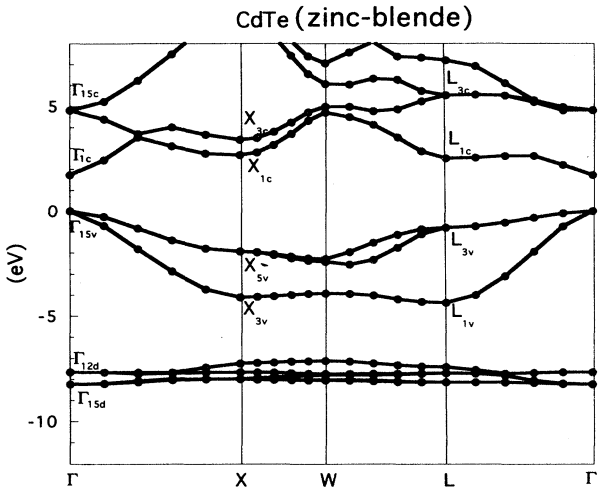

FIG. 7. Band structure of CdTe at the theoretical lattice constant ($a=6.478$ Å) using GDS/DFT with the $MS4^*$ basis.

(Ref. 63) result of 6.541 Å. We obtain a direct band gap of 1.72 eV, which is larger than the LAPW (Ref. 63) result of 1.44 eV and the experimental result of 1.59 eV.[60] This LDA band gap is larger than experiment because we neglect relativistic effects (which destabilizes the cation s level and stabilizes the anion p level) increasing the gap. In fact, inclusion of relativistic effects in the LDA reduces the gap to 0.58 eV,[64] much lower than the experimental result, as expected. Table XII reports the band structure at some high-symmetry points, leading to very good agreement with the LAPW. Figure 7 is the band structure of CdTe along some high-symmetry directions.

V. SUMMARY

We develop the GDS/DFT method for first-principles all-electron calculations of periodic systems using Gaussian-type basis sets. The applicability of this method for accurate large-scale calculations with Gaussian functions relies on three major features: (1) the design of an accurate grid; (2) the efficient dual-space approach for the construction of the Coulomb potential via the use of projection functions; and (3) the generalized conjugate gradient update of wave functions with preconditioning.

For large systems we expect the cost of calculating matrix elements to scale linearly, so that the computational costs of the conjugate gradients becomes dominant. Since Gaussian basis sets are typically 6–100 times smaller than plane-wave bases, we expect GDS/DFT to become much faster for computations of large-scale systems. Additional advantages are that all electrons can be included in the calculation, allowing all elements of the Periodic Table to be treated.

The accuracy of the grid is tested rigorously for molecular calculations where all the elements of the Fock matrix are compared with analytical results. The results are very encouraging (see Sec. II). With grid optimization (see Sec. II), GDS/DFT should be suitable for including nuclear relaxation. We are now in the process of implementing Car-Parrinello-type molecular dynamics[6] with the method proposed here.

To provide a variety of tests for GDS/DFT, we report calculations on both crystal and surface systems. These test show that GDS/DFT is accurate for systems with a variety of bonding characters.[67]

ACKNOWLEDGMENTS

This work was partially funded by the NSF (ASC 92-100368). Part of the computations were carried on the JPL Cray-YMP (under the Caltech-JPL supercomputing project) and on the Cray-YMP in Goddard space center. The facilities of the MSC are also supported by grants from DOE-AICD, Allied-Signal Corp., Asahi Chemical, Asahi Glass, Chevron Petroleum Technology, BF Goodrich, Xerox, Hughes Research Lab., Teijin Ltd., and the Beckman Institute.

APPENDIX: RECURSIVE RELATION FOR THE FOURIER TRANSFORM

The Fourier transform is used for the reciprocal-space calculation of the Coulomb potential due to the residual charges [see (17)]. The Gaussian functions is written as

$$\chi_{\mu q}=N_\mu x_q^{m_\mu} y_q^{n_\mu} z_q^{p_\mu} e^{-\zeta_\mu r_q^2} ,$$

where q denotes the center, $m_\mu+n_\mu+p_\mu=l$ (the angular momentum, e.g., $l=2$ for d functions), N_μ is a normalization constant, and ζ_μ is a real number. The general form for the Fourier transform of a pair of Gaussian functions is

$$\rho_{\mu q,\nu p}(\mathbf{G})=\int d^3r\, \chi_{\mu q}(\mathbf{r})\chi_{\nu p}(\mathbf{r})e^{i\mathbf{G}\cdot\mathbf{r}} \quad \text{(A1)}$$

where $\chi_{\mu q}$ is a Gaussian basis function on center q. The basic integral used in computing $\rho_{\mu q,\nu p}(\mathbf{G})$ is

$$I(G_x)=\int_{-\infty}^{\infty} dx\, e^{iG_x x}(x-x_q)^{m_\mu} e^{-\zeta_\mu (x-x_q)^2} \times (x-x_p)^{m_\nu} e^{-\zeta_\nu (x-x_p)^2} , \quad \text{(A2)}$$

where q and p denote the atoms to which the basis functions μ and ν (with exponents ζ_μ and ζ_ν) belong. In order to derive the recursion relation, we use the identity

$$\int_{-\infty}^{+\infty} dx \frac{\partial}{\partial_x}[e^{iG_x x}(x-x_q)^{m_\mu} e^{-\zeta_\mu (x-x_q)^2} \times (x-x_p)^{m_\nu} e^{-\zeta_\nu (x-x_p)^2}]=0 , \quad \text{(A3)}$$

which leads to

$$2\zeta_\mu I_{m_\mu+1,m_\nu}+2\zeta_\nu I_{m_\mu,m_\nu+1} =iG_x I_{m_\mu,m_\nu}+m_\mu I_{m_\mu-1,m_\nu}+m_\nu I_{m_\mu,m_\nu-1} . \quad \text{(A4)}$$

Second, from the identity $x_q - x_p = (x - x_p) - (x - x_q)$ and (A2), we have

$$(x_q - x_p) I_{m_\mu, m_\nu} = I_{m_\mu + 1, m_\nu} - I_{m_\mu, m_\nu + 1} \,. \tag{A5}$$

Combining (A4) and (A5) to eliminate $I_{m_\mu, m_\nu + 1}$ leads to the recursion relation

$$I_{m_\mu + 1, m_\nu} = \left[\frac{\zeta_\nu}{\gamma_{\mu\nu}} (x_q - x_p) + \frac{iG_x}{2\gamma_{\mu\nu}} \right] I_{m_\mu, m_\nu} + \frac{m_\mu}{2\gamma_{\mu\nu}} I_{m_\mu - 1, m_\nu} + \frac{m_\nu}{2\gamma_{\mu\nu}} I_{m_\mu, m_\nu - 1} \,, \tag{A6}$$

where $\gamma_{\mu\nu} = \zeta_\nu + \zeta_\mu$. The recursion relation to increment the value of m_ν is obtained from (A6) by exchanging indices.

*Present address: Schrödinger Inc., 80 S. Lake Ave. (Suite 735), Pasadena, CA 91101.

†Author to whom correspondence should be addressed.

[1]W. Kohn and L. J. Sham, Phys. Rev. **140**, A1133 (1965).

[2]P. J. Hay and W. R. Wadt, J. Chem. Phys. **82**, 270 (1985); W. R. Wadt and P. J. Hay, *ibid.* **82**, 284 (1985); P. J. Hay and W. R. Wadt, *ibid.* **82**, 299 (1985).

[3]T. H. Dunning, Jr. and P. J. Hay, in *Methods of Electronic Structure Theory,* edited by H. F. Schaefer III (Plenum, New York, 1977); R. Krishnan, J. S. Binkley, R. Seeger, and J. A. Pople, J. Chem. Phys. **72**, 650 (1980).

[4]M. P. Teter, M. C. Payne, and D. C. Allan, Phys. Rev. B **40**, 12 255 (1989).

[5]J. Ihm, A.Zunger, and M. L. Cohen, J. Phys. C **12**, 4409 (1979).

[6]R. Car and M. Parrinello, Phys. Rev. Lett. **55**, 2471 (1985).

[7]C. S. Wang and J. Callaway, Comput. Phys. Commun. **14**, 327 (1978); S. C. Erwin, M. R. Pederson, and W. E. Pickett, Phys. Rev. B **41**, 10437 (1990), and references therein; H. Kobayashi, D. R. Salahub, and T. Ito, J. Phys. Chem. **98**, 5487 (1994).

[8]D. R. Salahub, R. Fournier, P. Mlynarsky, I. Papai, A. St-Amant, and J. Ushio, in *Density Functional Methods in Chemistry,* edited by J. K. Labanowski and J. W. Andzelm (Springer-Verlag, Berlin, 1991); G. te Velde and E. J. Baerends, Phys. Rev. B **15**, 7888 (1991); J. W. Mintmire, Int. J. Quantum Chem. **S24**, 851 (1990); Volker Termath and Nicholas C. Handy, Chem. Phys. Lett. **230**, 17 (1994).

[9]M. Methfessel *et al.*, Phys. Rev. A **40**, 2009 (1989), and references therein.

[10]E. Wimmer, H. Krakauer, M. Weinert, and A. J. Freeman, Phys. Rev. B **24**, 864 (1981), and references therein.

[11]R. Yu, D. Singh, and H. Krakauer, Phys. Rev. B **43**, 6411 (1991).

[12]J. M. Soler and A. R. Williams, Phys. Rev. B **42**, 9728 (1990).

[13]S. Goedecker and K. Maschke, Phys. Rev. B **45**, 1597 (1992); P. E. Blöchl, *ibid.* **50**, 17 953 (1994).

[14]A. D. Becke, J. Chem. Phys. **88**, 2547 (1988).

[15]V. I. Lebedev, Sib. Math. Zh. **18**, 132 (1977), and references therein.

[16]S. Obara and A. Saika, J. Chem. Phys. **84**, 3963 (1986).

[17]M. P. Tosi, in *Solid State Physics,* edited by H. Ehrenreich and D. Turnbull (Academic, New York, 1964), Vol. 16, p. 102.

[18]D. J. Chadi and M. L. Cohen, Phys. Rev. B **8**, 5747 (1973).

[19]S. Froyen, Phys. Rev. B **39**, 3168 (1989).

[20]M. C. Payne, M. P. Teter, D. C. Allan, T. A. Arias, and J. D. Joannopoulos, Rev. Mod. Phys. **64**, 1045 (1992).

[21]T. P. Hamilton and P. Pulay, J. Chem. Phys. **84**, 5728 (1986).

[22]L. Hedin and B. I. Lundquist, J. Phys. C **4**, 2064 (1971).

[23]P. Pavone, K. March, O. Schütt, W. Windl, D. Strauch, P. Giannozzi, and S. Baroni, Phys. Rev. B **48**, 3156 (1993).

[24]G.B. Bachelét, H. S. Greenside, G. A. Baraff, and M. Schlüter, Phys. Rev. B **24**, 4745 (1981).

[25]J. R. Chelikowsky and S. G. Louie, Phys. Rev. B **29**, 3470 (1984).

[26]*The Properties of Diamond,* edited by J. E. Field (Academic, London, 1979).

[27]S.-H. Wei, H. Krakauer, and M. Weinert, Phys. Rev. B **32**, 7792 (1985).

[28]W. E. Pickett and C. S. Wang, Phys. Rev. B **30**, 4719 (1984).

[29]L. J. Sham and M. Schlüter, Phys. Rev. Lett. **51**, 1888 (1983).

[30]W. A. Goddard III, J. J. Barton, A. Redondo, and T. C. McGill, J. Vac. Sci. Technol. **15**, 1274 (1978).

[31]S. Y. Tong, A. R. Lubinsky, B. J. Mrstik, and M. A. Van Hove, Phys. Rev. B **17**, 3303 (1978).

[32]R. Chang and W. A. Goddard III, Surf. Sci. **144**, 311 (1984).

[33]A. K. Rappè and W. A. Goddard III (unpublished).

[34]D. M. Ceperley and B. I. Alder, Phys. Rev. Lett. **45**, 566 (1980); J. P. Perdew and Alex Zunger, Phys. Rev. B **23**, 5048 (1981).

[35]L. I. Berger and B. R. Pamplin, in *Handbook of Chemistry and Physics,* 74th ed., edited by David R. Lide and H. P. R. Frederikse (Chemical Rubber, Boca Raton, FL, 1993), pp. 12–79.

[36]G.-X. Qian, R. M. Martin, and D. J. Chadi, Phys. Rev. B **37**, 1303 (1988).

[37]A. Rubio, J. L. Corkill, M. L. Cohen, E. L. Shirley, and S. G. Louie, Phys. Rev. B **48**, 11 810 (1993).

[38]J. E. Northrup, Phys. Rev. B **44**, 1349 (1991).

[39]S. Y. Tong, W. N. Mei, and G. Xu, J. Vac. Sci. Technol. B **2**, 393 (1984).

[40]C. B. Duke, S. L. Richardson, A. Paton, and A. Kahn, Surf. Sci. **127**, L135 (1983).

[41]S. Koizumi, T. Murakami, T. Inuzaka, and K. Suzuki, Appl. Phys. Lett. **57**, 563 (1990).

[42]L. F. Allard, A. K. Datye, and T. A. Nolanm, Ultramicroscopy **37**, 153 (1991).

[43]*Semiconductors. Physics of Group IV Elements and III-V Compounds,* edited by O. Madelung, Landolt-Börnstein, New Series, Group III, Vol. 17, Pt. a (Springer-Verlag, New York, 1982), p. 148.

[44]R. M. Wentzcovitch, K. J. Chang, and M. L. Cohen, Phys. Rev. B **34**, 1071 (1986).

[45]J. A. Sanjuro, E. López-Cruz, P. Vogl, and M. Cardona, Phys. Rev. B **28**, 4579 (1983).

[46]C. A. Swarts, T. C. McGill, and W. A. Goddard III, Surf. Sci. **110**, 400 (1981).

[47]P. A. Heiney *et al.*, Phys. Rev. Lett. **66**, 2911 (1991).

[48]N. Troullier and J. L. Martins, Phys. Rev. B **46**, 1754 (1992).

[49]Y. Guo, N. Karasawa, and W. A. Goddard, Nature **351**, 464 (1991).
[50]E. L. Shirley and S. G. Louie, Phys. Rev. Lett. **71**, 133 (1992).
[51]T. Rabenau, A. Simon, R. K. Kremmer, and E. Sohmen, Z. Phys. B **90**, 69 (1993).
[52]T. Takahashi *et al.*, Phys. Rev. Lett. **68**, 1232 (1992).
[53]R. M. Lof, M.A. van Veenendaal, B. Koopman, H. T. Jonkman, and G. A. Sawatzky, Phys. Rev. Lett. **69**, 3924 (1992).
[54]T. Lei, T. D. Moustakas, R. J. Graham, Y. He, and S. J. Berkowitz, J. Appl. Phys. **71**, 4933 (1992); T. Lei, T. D. Moustakas, R. J. Graham, Y. He, and J. Scanlon, J. Appl. Phys. Lett. **59**, 944 (1992); C. R. Eddy, T. D. Moustakas, and J. Scanlon, J. Appl. Phys. **73**, 448 (1993).
[55]W. M. Yim and R. J. Paff, J. Appl. Phys. **45**, 1456 (1974).
[56]R. C. Powell, G. A. Tomash, Y.-W. Kim, J. A. Thornton, and J. E. Greene, in *Diamond, Silicon Carbide and Related Wide Band Gap Semiconductors,* edited by J. T. Glass, R. Messier, and N. Fujimori, MRS Symposia Proceedings No. 162 (Material Research Society, Pittsburgh, 1990), p. 525.
[57]P. Perlin, C. Jauberthie-Carillon, J. P. Itie, A. San Miguel, I. Gorczyca, and A. Polian, Phys. Rev. B **45**, 83 (1992); P. Perlin, I. Gorczyca, N. E. Christensen, I. Grzegory, H. Teisseyre, and T. Suzuki, *ibid.* **45**, 13 307 (1992); H. Vollstädt, E. Ito, M. Akaishi, S. Akimoto, and O. Fukunaga, Proc. Jpn. Acad. B **66**, 7 (1990); M. Ueno, A. Onodera, O. Shimomura, and K. Takemura, Phys. Rev. B **45**, 10 123 (1992).
[58]W. R. L. Lambrecht and B. Segal, Phys. Rev. B **43**, 7070 (1991).
[59]R. Pandey, A. Sutjianto, M. Seel, and J. E. Jaffe, J. Mater. Res. **8**, 1922 (1993).
[60]*Semiconductors. Physics of Group IV Elements and III-V Compounds* (Ref. 43).
[61]P. E. van Camp. V. E. van Doren, and J. T. Devreese, Phys. Rev. B **44**, 9056 (1991); Solid State Commun. **81**, 23 (1992).
[62]See, for example, N. R. Taskar, I. B. Bhat, K. K. Parat, S. K. Ghandhi, and G. J. Scilla, J. Vac. Sci. Technol. B **9**, 1705 (1991); J. M. Arias, M. Zandian, R. Zucca, and R. E. DeWames, Appl. Phys. Lett. **58**, 2806 (1991).
[63]S. H. Wei and A. Zunger, Phys. Rev. B **37**, 8958 (1988).
[64]X. J. Chen, X. L. Hua, J. Hu, J.-M. Langlois, and W. A. Goddard III (unpublished).
[65]G. B. Bachelét, D.R. Hamann, and M. Schlüter, Phys. Rev. B **26**, 4199 (1982).
[66]$|e|=1$, $\hbar=1$, and $m_e=1$. Thus the unit of length in bohr ($1a_0=0.529\,17$ Å) and the unit of energy in hartree (1 hartree $=27.2116$ eV $=627.51$ kcal/mol).
[67]Diamond is a covalently bonded system; III-V nitrides have both covalent and ionic characters; surface electronic structures usually have both ionic bonding character as well as covalent bonding character.